Structure of amorphous Cu_2GeTe_3 and the implications for its phase-change properties

Jens R. Stellhorn,[1,2,3,*] Benedict Paulus,[1,4] Shinya Hosokawa,[1,4] Wolf-Christian Pilgrim,[4] Nathalie Boudet,[5] Nils Blanc,[5] Hiroyuki Ikemoto,[6] Shinji Kohara,[7,8,9] and Yuji Sutou[10]

[1]*Department of Physics, Kumamoto University, Kumamoto 860-8555, Japan*
[2]*Deutsches Elektronen-Synchrotron DESY, 22603 Hamburg, Germany*
[3]*Department of Applied Chemistry, Hiroshima University, Hiroshima 739-8527, Japan*
[4]*Department of Chemistry, Philipps University of Marburg, 35032 Marburg, Germany*
[5]*Université Grenoble Alpes, CNRS, Grenoble INP, Institut Néel, 38000 Grenoble, France*
[6]*Department of Physics, University of Toyama, Toyama 930-8555, Japan*
[7]*Research Center for Advanced Measurement and Characterization, National Institute for Materials Science (NIMS), Hyogo 679-5148, Japan*
[8]*Center for Materials Research by Information Integration (CMI^2), Research and Services Division of Materials Data and Integrated System (MaDIS), National Institute for Materials Science (NIMS), Ibaraki 305-0047, Japan*
[9]*PRESTO, Japan Science and Technology Agency, Tokyo 102-0076, Japan*
[10]*Department of Materials Science, Tohoku University, Sendai 980-8579, Japan*

(Received 5 February 2020; revised manuscript received 15 March 2020; accepted 5 June 2020; published 25 June 2020)

The structure of amorphous Cu_2GeTe_3 is investigated by a combination of anomalous x-ray scattering and extended x-ray absorption fine-structure experiments. The experimental data are analyzed with reverse Monte Carlo modeling, and they are interpreted in terms of short-range-order parameters as well as by using ring statistics and persistent homology to study the intermediate-range order. Based on this information, the structural relationship of the amorphous phase to the corresponding crystal is discussed. It is found that the amorphous network can be rationalized by small atomic displacements of the crystal structure, directed toward the intrinsic void regions. This structural similarity establishes the possibility of a fast phase-change process. On the other hand, the atomic rearrangements also lead to the formation of new chemical bonds and to distortions on the intermediate-range-order level. These are realized by a collapse and contraction of the strict hexagonal ring arrangements of the crystal and by the formation of small, triangular rings as well as Cu cluster configurations. These structural features allow for a new understanding of the phase-change property contrast of this material, especially concerning the density change and the optical contrast.

DOI: 10.1103/PhysRevB.101.214110

I. INTRODUCTION

Phase-change materials (PCMs) utilize the reversible change from an amorphous phase to a crystalline phase to encode binary data [1,2]. The readability of the stored data is guaranteed by the pronounced differences in the electrical and/or optical properties of both phases. Cu_2GeTe_3 (CGT) is a new PCM that is expected to be used for a next generation of (nonvolatile) data storage devices [3,4]. The CGT crystalline film was found to be amorphized by laser irradiation with a lower power and shorter pulse width than currently employed and widely studied GeSbTe alloys, which are essential properties to achieve rapid data recording and low power consumption in PCMs [1,4,5]. Further differences between these PCM systems are a reverse density change, i.e., amorphous CGT is actually denser than the crystal, and a negative optical contrast, i.e., the reflectivity of the crystalline phase is lower than that of the amorphous phase [4], contrary to GeSbTe [5,6].

Structurally, there is another fundamental distinction in the two PCM systems: The crystalline phase in GeSbTe is generally characterized by octahedrally bonded cubic structures [1,7]. The transition to the amorphous phase involves the reorganization of the local environment, particularly for the Ge atoms, of which a considerable fraction form tetrahedral arrangements. This substantial change in the bonding scheme significantly affects the optical properties of the material and establishes the optical contrast in GeSbTe. Note that the special bonding situation in the crystalline phase has been studied extensively, and was dubbed "resonant" [6,8] or "meta-valent" bonding [9,10], although these concepts are controversial; cf., Refs. [11,12].

On the other hand, the crystal structure of CGT is exclusively composed of tetrahedral configurations: the unit cell of CGT consists of a three-dimensional arrangement of slightly distorted corner-sharing $CuTe_4$ and $GeTe_4$ tetrahedra, with the space group $Imm2$ [13]. The complete absence of octahedral motifs implies that structural changes related to the optical contrast in CGT are fundamentally different from GeSbTe, and alternative explanations must be considered to explain its performance as a PCM. The crucial point then lies in the

*stellhoj@hiroshima-u.ac.jp

understanding of the structure of the corresponding amorphous phase. There, however, the state of research is inconsistent: different average coordination numbers have been reported by x-ray diffraction in combination with x-ray absorption fine structure (XAFS) measurements [14], by XAFS investigations alone [15], and by *ab initio* molecular dynamics (AIMD) simulation [16–18].

The experimental results [14] so far indicate that all atoms are roughly fourfold-coordinated, which would constitute a large similarity to the tetrahedral crystal structure. This structural model certainly helps to explain the fast phase-change process in this material, but fails to describe the phase-change property contrast such as the increased density and reflectivity by amorphization. AIMD simulations find much larger coordination numbers of Ge and Cu, with values exceeding 6 for Cu and about 4.5 for Ge [16]. Agreement is reached only on two points, namely the unusually large average coordination numbers for Cu and Te atoms, and the existence of a significant number of homopolar bonds for Cu-Cu pairs (so called "wrong" bonds, which do not exist in the crystalline phase).

Apart from the investigation of nearest-neighbor arrangements, it is possible to analyze the intermediate-range topology of a system by more advanced methods, including ring statistics calculations and persistent homology. Ring statistics offer the possibility to characterize the topological connectivity of network structures. For comparison, the ring structures in GeSbTe have been investigated both experimentally [19] and theoretically by *ab initio* simulations [20–22]. In general, the fast phase-change ability of GeSbTe was attributed to a strong preference of (alternating) even-fold rings, facilitating the phase transition to the crystal with a similar ring structure. For the ring statistics of CGT, there are only theoretical investigations available so far [16,17]. The reported ring structures are strikingly different from the known features of GeSbTe, especially concerning a large contribution of threefold rings. However, experimental support for this finding is still missing.

Furthermore, a persistent homology analysis offers the possibility to extract multiscale information about topological features of an atomic configuration. The homology is expressed as a two-dimensional (2D) histogram called a persistence diagram (PD) [23–26]. These diagrams capture specific shapes in the data, e.g., one-dimensional linkages, such as ring structures, for multiple length scales. The PDs encode certain characteristics of such ring structures, e.g., the maximum distance between two adjacent atoms in the rings and the size of the rings. More detailed descriptions of this method can be found in the indicated references, along with examples for Cu-Zr [24] and SiO_2 [25] glasses. Persistent homology allows for an extended view into the intermediate-range order beyond ring statistics calculations.

A powerful method to obtain structural data with information on the short- and intermediate-range order is anomalous x-ray scattering (AXS), especially in combination with extended XAFS experiments. The aim of this article is to use this extensive experimental approach, analyzing the datasets with reverse Monte Carlo (RMC) modeling, and subsequently evaluating the atomic configuration with the above-mentioned procedures, in order to build a suitable model for the amorphous phase of CGT. The model should provide insight into the property contrast between the crystalline and amorphous phase, and thus ultimately into the phase-change process of this exotic phase-change material.

II. EXPERIMENT

The amorphous CGT sample was prepared by radiofrequency sputtering deposition from GeTe and CuTe alloy targets on SiO_2(20 nm)/Si(0.7 mm) substrates. Details on the sample preparation are given elsewhere [4,27]. The AXS experiments were performed at the beamline BM02 of the European Synchrotron Radiation Facility (ESRF). Incident energies for the measurements were selected 20 and 200 eV below the Cu and Ge K edges, as well as 30 and 300 eV below the Te K edge, respectively. The experiments were performed in transmission geometry using a container cell with 7 μm Kapton windows and appropriate thicknesses for each investigated energy region. A bent graphite analyzer crystal was used in the detecting system, which provides a good energy resolution to discriminate most of the fluorescent x-rays [28]. The data were corrected for absorption effects and Compton scattering, and normalized using the Krogh-Moe-Norman method [29,30]. Further details on the theoretical and experimental background of AXS can be found elsewhere [28,31–34]. The XAFS experiments were conducted at BL12C of the Photon Factory in the High Energy Accelerator Research Organization (KEK-PF), in fluorescence mode. The incident x-ray intensity was measured using an ion chamber, and the fluorescent x-ray intensity from the sample was detected using a 19-channel pure Ge solid state detector. XAFS functions were determined near the K edges of Cu and Ge. The backscattering factors for the data analysis were calculated with the FEFF program package [35].

Methodologically, AXS utilizes the anomalous variation of the atomic form factor f of a specific element in the vicinity of an x-ray absorption edge [31]. The experimentally accessible information is the differential structure factors $\Delta_k S(Q)$:

$$\Delta_k S(Q) = \frac{\Delta_k[C \cdot I(Q, E_1, E_2)] - \Delta_k[\langle f^2\rangle - \langle f\rangle^2]}{\Delta_k[\langle f\rangle^2]}, \quad (1)$$

which are functions of the scattering vector Q, calculated from the difference (Δ_k) of two scattering experiments with intensities $I(Q, E)$ conducted at energies E_1 and E_2 close to the absorption edge of element k. C denotes the normalization factor. The $\Delta_k S(Q)$ functions contain structural information specifically related to the element k. The relative increase of this information can be illustrated by the AXS weighting factors W_{ij}^k, which are defined as

$$W_{ij}^k(Q, E_1, E_2) = x_i x_j \frac{\Delta_k[f_i f_j]}{\Delta_k[\langle f^2\rangle]} \quad (2)$$

for all elements i, j, with the atomic concentrations x_i, x_j. They describe the relative weighting of the partial contributions $S_{ij}(Q)$ to the differential structure factor:

$$\Delta_k S(Q) = \sum_{i,j} W_{ij}^k(Q, E_1, E_2) S_{ij}(Q). \quad (3)$$

The weighting factors for CGT are summarized in Table I. Note that the W_{ij}^k have a small Q dependence, and they are

TABLE I. Weighting factors W_{ij}^k in CGT at 1.9 Å^{-1} near the first $S(Q)$ maximum, in percent.

	Cu-Cu	Cu-Ge	Cu-Te	Ge-Ge	Ge-Te	Te-Te
$S(Q)$	6.5	7.0	30.9	1.9	16.8	36.9
$\Delta_{Cu}S(Q)$	20.3	13.1	65.6	0.2	0.9	−0.1
$\Delta_{Ge}S(Q)$	−1.7	24.3	−4.0	11.5	68.3	1.6
$\Delta_{Te}S(Q)$	0.0	0.0	25.8	0.0	14.0	60.2

given here exemplarily for $Q = 1.9$ Å^{-1}, i.e., at the first $S(Q)$ maximum position. The table illustrates the element selectivity of AXS: correlations related to the element k are highly enhanced in the respective $\Delta_k S(Q)$. In particular, the contributions of "wrong" bond correlations are enhanced by AXS in the respective $\Delta_k S(Q)$, e.g., Cu-Cu to 20.3% in $\Delta_{Cu}S(Q)$, and Cu-Ge to 24.3% and Ge-Ge to 11.5% in $\Delta_{Ge}S(Q)$. Furthermore, although the information content on Ge correlations is low in the total $S(Q)$, where Te-related weighting factors represent the major contribution and make up about 84% of the scattering signal, AXS strongly enhances the weighting of the Ge-related contributions in $\Delta_{Ge}S(Q)$, where all other correlations (in particular Cu-Te and Te-Te) are highly suppressed. The obtained information content thereby provides a reasonable basis for a structural model, especially with respect to distinguishing the correlations of Cu and Ge.

The experimental AXS and XAFS data are displayed in Fig. 1 with black symbols. The $\Delta_k S(Q)$ functions generally exhibit similar features, with two main peaks at about $Q_1 = 1.9$ Å^{-1} and $Q_2 = 3.2$ Å^{-1}, with a nearly constant peak height of the latter over all datasets, and distinct intensities of the Q_1 peak with $\Delta_{Te}S(Q_1) > S(Q_1) > \Delta_{Cu}S(Q_1) > \Delta_{Ge}S(Q_1)$. The AXS and XAFS datasets are then fed into a reverse Monte Carlo procedure, which models the real sample by an ensemble of atoms as hard spheres in a simulation box. From the atomic positions in the computer-generated ensemble, the partial pair correlation functions $g_{ij}(r)$ and, by inverse Fourier transform, the respective partial structure factors $S_{ij}(Q)$ are calculated. The latter are summed with appropriate weighting factors [Eqs. (2) and (3)] to calculate the RMC-total and differential structure factors, $S^{RMC}(Q)$ and $\Delta_k S^{RMC}(Q)$. In a similar way, it is possible to calculate the RMC-XAFS functions $\chi^{RMC}(k)$ by providing the backscattering coefficients for the Fourier transform (calculated, e.g., by the FEFF program). The RMC-functions are compared with the experimental data, i.e., $S^{RMC}(Q)$ with $S^{exp}(Q)$, $\chi_k^{RMC}(k)$ with $\chi_k^{exp}(k)$, etc. Then, in each simulation step, individual atoms are moved randomly using a METROPOLIS algorithm, and atomic moves are accepted or declined so as to minimize the difference between the experimental data and those computed from the RMC configuration [36,37].

We employed the RMC_POT package for our simulations [36,37]. An input configuration of 10 000 atoms with proper stoichiometry and with an initial random distribution of the atoms in a box corresponding to the number density of 0.0385 Å^{-3} was used. Minimal interatomic distances for the individual correlations Cu-Cu, Cu-Ge, Cu-Te Ge-Ge, Ge-Te, and Te-Te were set to 2.45, 2.35, 2.35, 2.35, 2.35, and 2.45 Å,

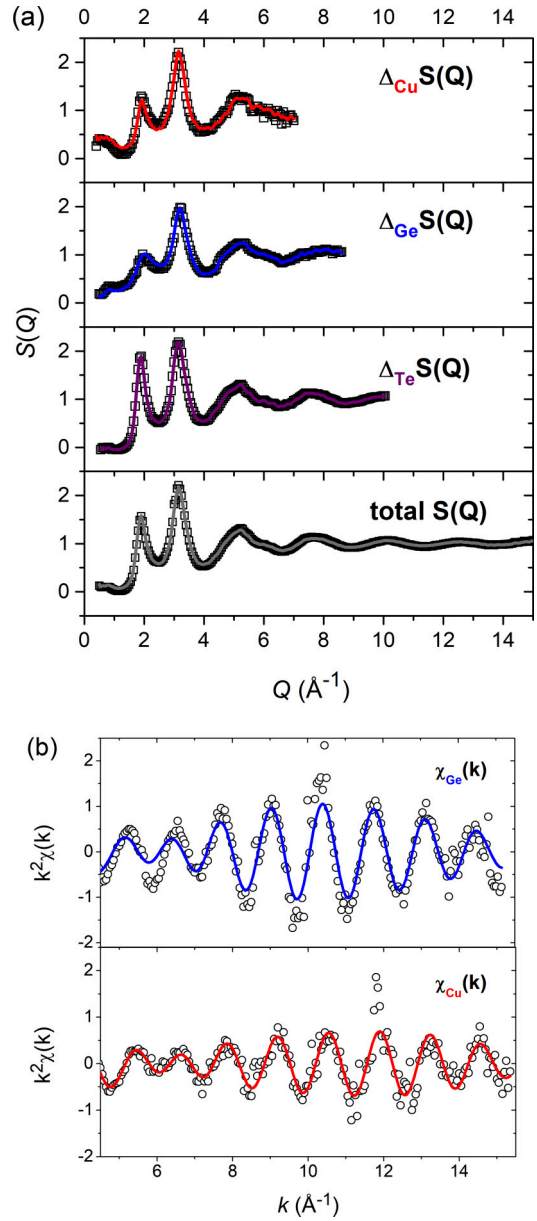

FIG. 1. Experimental data: (a) AXS and (b) XAFS. Black symbols are experimental data. RMC fits are displayed as colored lines, with data acquired near the absorption edges of Te (purple), Ge (blue), and Cu (red); the total $S(Q)$ is shown in gray.

respectively. These distances were chosen near the values for the respective sums of the covalent radii [38], and they were adjusted to fit the first coordination shells adequately. To evaluate the reliability of the RMC configuration and the statistical error connected with the RMC modeling, a set of 10 independent RMC calculations with the same parameters was determined. In this respect, the use of multiple experimental datasets is essential to generate a unique structural solution, as was stressed, e.g., for the GeSbTe system [39]. The present approach, with four different x-ray scattering and two different XAFS datasets, and a large simulation box with 10 000 atoms, leads to solutions with small standard deviations. The resulting RMC fits are illustrated in Fig. 1 with colored lines;

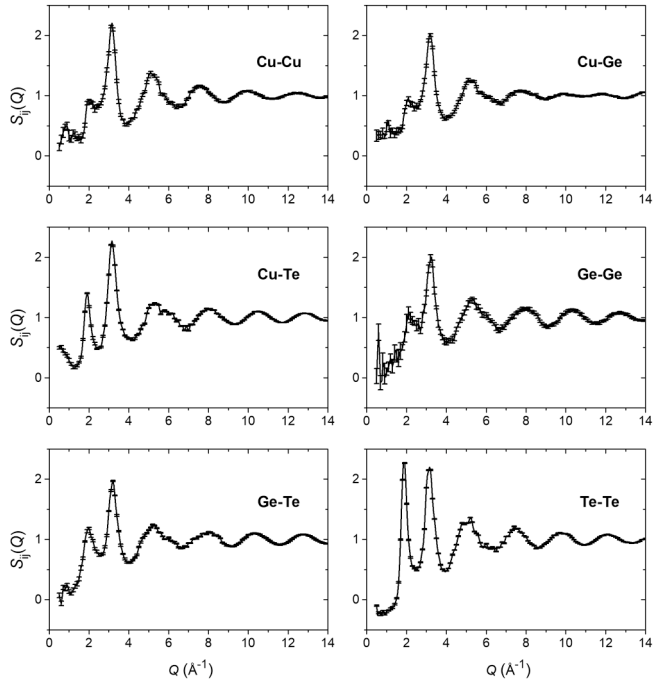

FIG. 2. RMC results for the partial structure factors $S_{ij}(Q)$ in the present model. The lines represent the average over the set of RMC calculations, which have standard deviations as indicated by the error bars.

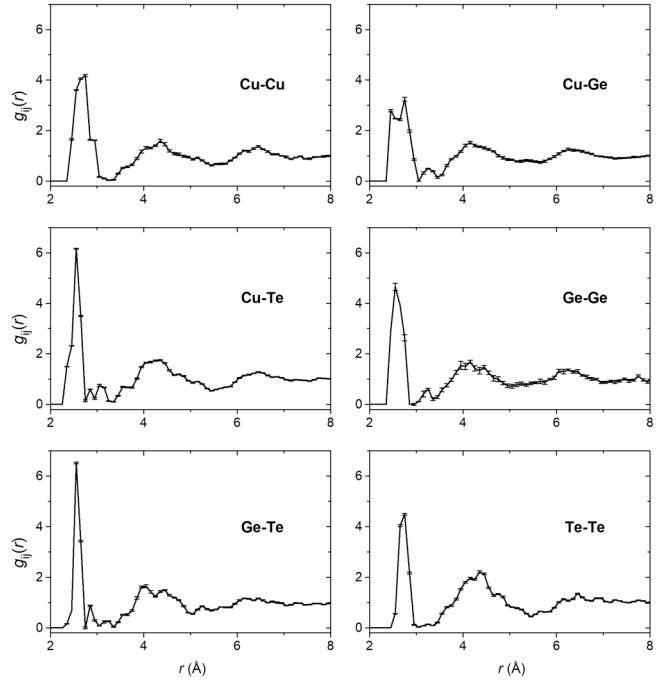

FIG. 3. RMC results for the partial pair correlations functions $g_{ij}(r)$ in the present model. The lines represent the average over the set of RMC calculations, which have standard deviations as indicated by the error bars.

the statistical uncertainty of the fits is smaller than the size of the symbols used to represent the experimental data.

III. RESULTS

From the RMC generated models, the six independent correlations of element pairs in CGT are calculated. Figures 2 and 3 give an overview of all $S_{ij}(Q)$ and the corresponding pair correlation functions $g_{ij}(r)$ obtained from the RMC simulation. The partial structure factors in Fig. 2 in general show similar forms with two main peaks at about $Q_1 = 1.9$ Å^{-1} and $Q_2 = 3.2$ Å^{-1}. While the peak height of the Q_2 signal is almost the same in each $S_{ij}(Q)$, the height of the Cu-Cu, Cu-Ge, and Ge-Ge Q_1 signal is strongly reduced. The $g_{ij}(r)$ in Fig. 3 overall also exhibit similar features. The first and second peaks are located at about $r_1 = 2.6$ Å and $r_2 = 4.2$ Å, respectively, although the values slightly change depending on the elemental pairs.

The average bond lengths were extracted from the pair correlations as average values of $g_{ij}(r)$ in the first-neighboring regions below the first minimum at around 3.0 Å, similar to the approach described in Ref. [40]. They are listed in Table II, in comparison with reference data from other studies and the corresponding values for the CGT crystal. It is notable that—within the precision of the experimental methods—interatomic distances in the amorphous phase of CGT do not differ largely from the corresponding crystalline phase (for the bonds that are present in the crystal): The heteropolar Cu-Te bonds are located at about 2.55 Å, in reasonable agreement with previous theoretical results [16,17] (see the supplementary materials of Ref. [16] for details), and in good agreement with previous experimental data [14,15] within the experimental error. The Ge-Te bond is slightly elongated compared to the crystal, with about 2.60 Å in the present approach. This is in good agreement with other experimental results [14,15], but distinctly shorter than the theoretical data [16,17], although the most recent AIMD study [18] reports somewhat shorter distance compared to the others.

In addition, a large number of homopolar "wrong" bonds is observed, with comparably long distances for Cu-Cu and Cu-Ge of about 2.65 Å. Shorter bonds are obtained for Ge-Ge of 2.59 Å, which is larger than the previous RMC result [14], but again shorter than the theoretical data [16–18]. Finally, the Te-Te homopolar bond length of 2.73 Å is shorter than the previous data, especially considering AIMD approaches [16–18].

The partial and total coordination numbers extracted from Fig. 3 are tabulated in Table III. Cutoff distances for the

TABLE II. Average bond lengths in Å for each correlation i-j, in comparison with other studies. For reference, the average distances in the crystal are also given.

	Cu-Cu	Cu-Ge	Cu-Te	Ge-Ge	Ge-Te	Te-Te
Present	2.68	2.65	2.56	2.59	2.60	2.73
XAFS [15]	2.60	2.57	2.58		2.60	
XAFS, RMC [14]	2.58		2.55	2.48	2.61	2.75
AIMD [16]	2.59	2.51	2.63	2.96	2.80	2.98
AIMD [17]	2.56	2.48	2.60	2.60	2.78	3.00
AIMD [18]	2.61	2.45	2.61	2.59	2.73	2.91
Crystal [13]			2.61		2.51	

TABLE III. Partial and total coordination numbers of CGT in comparison with other studies. Partial coordinations ij are given for j atoms around i centers. For the present results, coordination numbers of all configurations obtained by RMC were averaged, with standard deviations of less than 0.013 for all values. Note that Ref. [14] reports estimates for the uncertainties in the partial coordination numbers of about ±0.3–0.6. For reference, the average coordination numbers in the crystal are also given.

	CuCu	CuGe	CuTe	GeCu	GeGe	GeTe	TeCu	TeGe	TeTe	N (Cu)	N (Ge)	N (Te)	$\langle N \rangle$
Present	1.86	0.81	2.31	1.61	0.77	1.96	1.54	0.65	2.04	4.98	4.34	4.23	4.50
XAFS, RMC [14]	2.20		1.86		1.52	2.51	1.39	0.99	1.72	4.06	4.03	4.10	4.08
AIMD [16]	2.34	0.62	3.70	1.25	0.12	3.09	2.48	1.09	0.60	6.67	4.47	4.18	5.06
AIMD [17]	1.86	0.29	3.60	0.58	0.38	2.73	2.40	0.91	0.35	5.75	3.68	3.66	4.36
AIMD [18]	1.94	0.62	3.39	1.25	0.52	2.83	2.26	0.94	0.62	5.96	4.59	3.82	4.66
Crystal			4.00			4.00	2.67	1.33		4.00	4.00	4.00	4.00

calculation of the coordination numbers were set to the first minimum in the pair correlation functions around 3.0 Å. For reference, the average coordination numbers in the crystal are given there as well. The local atomic environments from the present investigation are characterized by large average coordination numbers, which are at least equal to or exceed the crystal coordination number of 4, in particular the Cu coordination with $N(\mathrm{Cu}) = 4.98$. Notably, there are major contributions of homopolar "wrong" bonds, i.e., for $n_{\mathrm{CuCu}} = 1.86$, $n_{\mathrm{TeTe}} = 2.04$, $n_{\mathrm{GeCu}} = 1.61$, and $n_{\mathrm{GeGe}} = 0.77$.

At first glance, there are major differences between the present data and the previously published experimental reference [14]. To evaluate these differences, it should be considered that the RMC modeling by Jóvári *et al.* [14] relied on only the total structure factor and XAFS datasets. Furthermore, they excluded the formation of Cu-Ge bonds, as they were able to achieve reasonable fit qualities without this correlation.

The existence of these bonds is difficult to judge from only XAFS and total scattering data due to the similar backscattering parameters [41] of Ge and Cu and the small weighting factors of the related correlations in the total $S(Q)$ (see Table I). It is, however, substantiated by the theoretical studies, of which two [16,18] report a similar coordination number (0.62 versus 0.81 in our study). Furthermore, the extensive present approach combining total scattering, XAFS, and AXS data also indicates the presence of Cu-Ge bonds from the experimental data itself, because the fit qualities are markedly improved by including this bond. To elaborate on this, a separate RMC simulation was conducted, in which the formation of Cu-Ge bonds was excluded by raising the minimal interatomic distance of this atomic pair to 3.1 Å. This leads to an increase in particular for the goodness-of-fit value R_w of the $\Delta_{\mathrm{Ge}}S(Q)$ dataset, which increases by 33.6% (relative increase to the R_w value for the result shown in Fig. 1). To put this into perspective: when the Ge-Ge bond is excluded (which is generally accepted to be present in chalcogenide glasses like GeSbTe or CGT), the R_w value of $\Delta_{\mathrm{Ge}}S(Q)$ increases by 19.7% (which was ascertained in another independent RMC run).

The Cu environment is characterized by high coordination numbers for Cu-Cu of 1.8–2.3 in the experiment as well as in the simulations. The other main feature are Cu-Te bonds, although the coordination numbers found by experiments with 1.8–2.3 are much smaller than the theoretical values of 3.4–3.7, which would be very close to the coordination number in the crystal. Another important difference is found in the Te environment, where the Te-Te bond is clearly dominant with very high coordination numbers of 1.7–2.0 in the experimental studies. Although the simulations also find this correlation significant, much smaller values of 0.35–0.62 are reported. Concerning the total coordination numbers $N(i)$, the previous RMC result [14] emphasized that they are almost equal to the crystal values of 4 around all elements. In contrast, the present results considerably exceed 4, in particular the large coordination number of Cu, which is consistent with theoretical results [16–18].

Finally, it needs to be addressed how the apparent differences between the experimental and computational works can be rationalized, particularly concerning the lengths of the Ge-Te and Cu-Ge bonds, and the differences in the coordination numbers (especially the contributions of homopolar bonds). One notable aspect is the preparation route of the sample. For the experimental observations, samples are usually prepared by sputter-deposition and used in the as-deposited (AD) form, as was done in this work. Computational studies usually obtain the amorphous structure by a melt-quench (MQ) procedure with rapid quenching and a limited sample size (fewer than 200 atoms in Refs. [16–18]). Indeed, the difference between AD and MQ structures was also recognized as a possible reason for the differences between the computational and the experimental approach by Skelton *et al.* [16]. For the GeSbTe system, the possible effects concerned with different preparation routes have been analyzed computationally with a large system size (648 and 460 atoms, respectively) [42], and distinctly more homopolar bonds were found in the AD than in the MQ case. As a result of the different bonding geometries around Ge, the preparation route also has a small impact on the bond length of Ge-Te (i.e., there are more tetrahedral Ge atoms in the AD phase, which tend to be shorter than the bonds with octahedral angles). A similar study on the CGT system might provide useful information to reconcile the experimental and computational approaches.

IV. DISCUSSION

A. Short-range order in CGT

Despite the disagreements between the results of the present RMC approach and the reference data, some consistent observations can be made: Large average coordination numbers are found (see Table III), especially around Cu, and

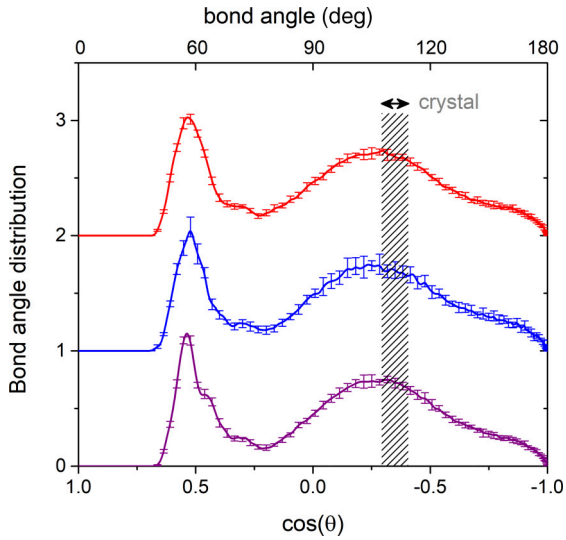

FIG. 4. Bond-angle distribution in amorphous CGT, around Cu (red), Ge (blue), and Te atoms (purple). The lines represent the average over the set of RMC calculations, which have standard deviations as indicated by the error bars. For reference, the angular distribution in the crystal is schematically shown as the dashed area.

there exists a large number of homopolar bonds, especially Cu-Cu (for every model) and Te-Te bonds (mainly in the experimentally obtained models). Together with the interatomic distances for the heteropolar bonds shown in Table II, which compared to the crystal structure are either similar (Cu-Te) or elongated (Ge-Te), respectively, we can establish a first key difference of CGT from comparable phase-change materials: in GeSbTe, for example, the shortening of the Ge-Te bond, in combination with a reduction in the coordination number, is a key motif of the phase-change process [7]. This is a clear indication for different structural features governing the phase-change process in these two materials.

These results also indicate a reason for the reverse density change in CGT [27] (compared to GeSbTe): when interatomic distances in the amorphous phase remain similar while the coordination numbers increase, the density of the material increases correspondingly.

B. Bond-angle distribution

By including the AXS data, reliable information on structural features beyond the coordination numbers and distances can be obtained. A detailed analysis of the present RMC model provides information on bond-angle distributions (BAD) and ring statistics of the network. We calculated the BAD around the individual elements, shown in Fig. 4. In general, broad distributions around 109° are observed for all correlations, corresponding to a distorted tetrahedral coordination. This correlates with the large number of fourfold-coordinated atoms, and it shows a considerable similarity to the crystal structure, where only tetrahedral configurations are found, though with a much narrower distribution (104°–114°, dashed area in Fig. 4).

In addition, peaks around 60° are found and are preferably connected with Cu-related correlations. This result is

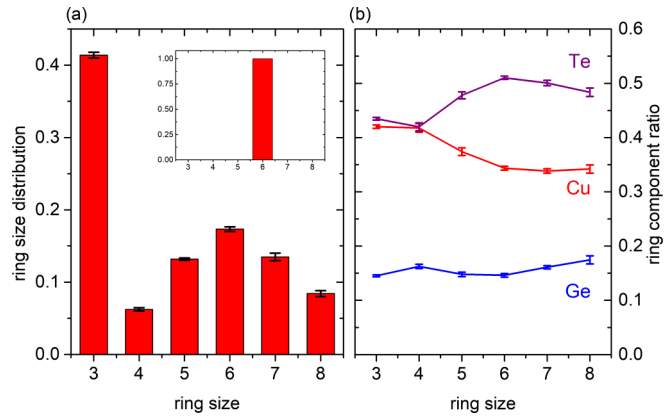

FIG. 5. Ring statistics in amorphous CGT (a) and the composition of the rings (b). The inset in (a) visualizes the sixfold rings in the crystal structure. The colors in (b) denote Cu (red), Ge (blue), and Te atoms (purple). The ring statistics and ring compositions were averaged over the set of RMC calculations, which have standard deviations as indicated by the error bars.

consistent with theoretical studies [16,17]. In their AIMD study, Chen *et al.* [17] attribute the 60° angles to mainly Cu-Cu-*X* and Cu-Te-*X* correlations. In their simulation, Ge-related bonds tend to form bond angles of preferably >80°, which is an apparent difference from our results. We relate this difference to the dominance of the Ge-Te correlation in Ref. [17], which tends to be realized with tetrahedral arrangements (like in the crystal structure of CGT), whereas we find dominating contributions of "wrong" bonds of Ge-Cu and Ge-Ge. Furthermore, the comparably low number of 90° angles is a striking difference from GeSbTe-based PCMs [21,39,43], and again demonstrates that the amorphous phases of CGT and GeSbTe systems are dominated by very different structural motifs.

C. Ring statistics

The BAD features can be understood by considering the rings statistics, which were calculated using the R.I.N.G.S. program [44]. A "ring" is defined as a closed path of bonds originating from and leading back to the same atom. For the ring statistics analysis, irreducible rings were searched in the amorphous network, i.e., closed paths that cannot be decomposed into smaller rings. The results are shown in Fig. 5.

The rings found in the crystal structure are connected hexagonal boat rings consisting of 2 Cu, 1 Ge, and 3 Te atoms. In the amorphous phase, a broad distribution of ring structures is found, with a shallow maximum for six-membered rings, as shown in Fig. 5(a). Furthermore, a large number of threefold rings is found, which corresponds to the peak around 60° in the BAD. The experimental ring statistics can be compared with AIMD results [17], where a similarly strong contribution of threefold rings is observed, but the number of sixfold rings is considerably smaller. We attribute this disagreement mainly to the difficulty to treat intermediate-range dispersion forces in the computational studies. Two of the three reference AIMD studies on CGT do not include a correct treatment of intermediate-range dispersion forces. The

dispersion correction was recently shown to have a significant impact especially on the ring structures in chalcogenide glasses from *ab initio* simulations [45]. Notably, the latest AIMD study [18] includes a Grimme-type dispersion correction [46], and found an increased number of 6-rings in amorphous CGT.

For more details on the network, we analyzed the composition of the rings, as shown in Fig. 5(b). The figure displays the relative ratio of the elements in the n-fold rings as a function of the ring size. A high component ratio is found for Cu atoms with about 40% in small rings. The Cu ratio decreases with the ring size, but remains above 33% throughout the ring sizes under consideration. The Cu atoms are gradually exchanged for Te, which increases from about 40% in small rings to about 50% in the larger rings. The component ratio of Ge of about 17% does not vary widely over the observed ring sizes, and corresponds well to the relative concentration.

To summarize the information from Fig. 5, the dominating features of the ring distribution are threefold and sixfold rings. Cu is found in all ring structures to a large degree, exceeding the expectation from its relative concentration (33%). This finding agrees well with the high coordination number of the Cu atoms, and is qualitatively in line with the AIMD investigations [18]. We can also indicate the composition of typical building blocks of the ring structures (given as a fraction of each n-fold ring distribution):

$n = 3$: $CuTe_2$ (27.1%), Cu_2Te (20.6%), CuGeTe (16.4%), and Cu_3 (7.0%).

$n = 4$: Cu_2Te_2 (55.3%) and $CuTe_3$ (22.8%).

$n = 5$: Cu_2GeTe_2 (29.3%), Cu_3GeTe (17.6%), and $CuGe_2Te_2$ (14.1%).

$n = 6$: Cu_2GeTe_3 (48.9%) and Cu_3GeTe_2 (16.2%).

Most of these buildings blocks cannot be realized without the formation of "wrong" bonds of Cu-Ge, Cu-Cu, or Te-Te, except for Cu_2Te_2 and Cu_2GeTe_3, the latter being the only ring structure in the crystalline phase.

At this point, we can again compare the situation of CGT with the traditional GeSbTe-based PCMs, which show a markedly different ring distribution. There, the crystal phase is (majorly) composed of 90° bond angles and alternating fourfold rings, and the resonant bonding via p-orbitals plays an important role for the stability and the optical properties [6,9]. The corresponding amorphous phase is supposed to be dominated by strictly alternating (i.e., *ABAB* ordered, with $A =$ Ge,Sb and $B =$ Te) [20,21] and even-membered ring structures (especially 4-rings) [19]. An AXS study also corroborates the importance of these 4-rings, though it emphasizes their puckered shape, with an impact on the electronic structure [47]. The fast phase-change in GeSbTe is then attributed to the structural similarity of the amorphous and crystalline networks [19]. The ring statistics of CGT apparently require a different explanation, and again emphasize the need for a new model to understand the relationship between the crystalline and amorphous phases.

D. Persistent homology analysis

The next level of structural order can be visualized by a topological analysis based on persistent homology. In this approach, persistence diagrams are used to visualize the persistent homology as a 2D histogram, which can extract multiscale topological features, such as (multiscale) ring structures. For the construction of the PD, an input configuration of a set of atomic coordinates is used (here: the atomic configuration obtained from RMC), and for every atom, a sphere with a radius α is constructed. The radius is then gradually increased, and at certain values $\alpha = b_k$, the formation of a closed ring k will be observed (birth). Increasing α further, a certain value $\alpha = d_k$ will be found, at which this ring disappears (death). The persistence diagram is a histogram of the birth-death plane of rings at the (b_k, d_k) coordinates. In this representation, the birth coordinate b_k is a measure for the longest distance between two adjacent atoms in the ring, and the death coordinate d_k indicates the size of the ring. Further details and visualizations of the method are given elsewhere [23–26].

The PD's for CGT are displayed in Fig. 6 for the configuration of the crystalline phase (a)–(d) based on a model of the crystal unit cell, and for the amorphous phase (e)–(h) from the present model. The dimensions of the birth and death scales are expressed in the form of distances, i.e., the birth value directly signifies the maximum interatomic distance of the ring (in Å). We can understand the PDs for the crystal (a)–(d) straightforwardly: There are few Ge atoms in the unit cell, so that one-dimensional linkages are only found at comparably long birth/death distances for the Ge-centered PD. Figure 6(a) was extended beyond the birth/death distance of 6 Å (to which the other PDs are limited) to show the first signals in this diagram. Cu features in (b) are related to trigonal structures formed by the two Cu atoms located within the hexagonal boat ring of CGT and a bridging Cu atom, which is bound to one of the Te atoms of this ring, as visualized by the inset schematic in (b). The birth distance corresponds to the Cu-Cu distance of 4.1–4.4 Å in the crystal. When both Ge and Cu atoms are selected (c), predominantly the trigonal structures within the hexagonal CGT ring are found, in addition to the structures realized in the PD of (b), corresponding to the Cu-Ge distance of about 4.1 Å. The Te features (d) are also determined by the trigonal structures of the Te atoms in the CGT ring. The signals in the PD are again distributed over a small area due to the different Te-Te distances in the crystal of about 4.1–4.36 Å.

The PDs of the amorphous phase, in contrast, do not exhibit the strongly confined features that are common for the crystalline phase. Instead, they are dominated by broad distributions and curvilinear streaks located close to the diagonal line, which are flattening out toward short birth values. These features are typical for the PDs of amorphous structures (in contrast to, e.g., crystals) [24]. Again, similar to the crystalline phase, there are few and weakly pronounced features in the Ge-centered distribution (e). The other amorphous PDs (f)–(h) in general display two distinct regions: The first is situated at short birth values (2.5–3.2 Å, region I) close to the average bond distances of the respective correlations, and a second region at longer birth values (3.5–5.5 Å, region II).

The region I at small birth distances can be further distinguished into (A) a high intensity "island" at low death values, and (B) a long, linear distribution at constant birth values. The high intensity island (I-A) is strongest for Cu (f) and mixed Ge and Cu centers (g). The short birth/death

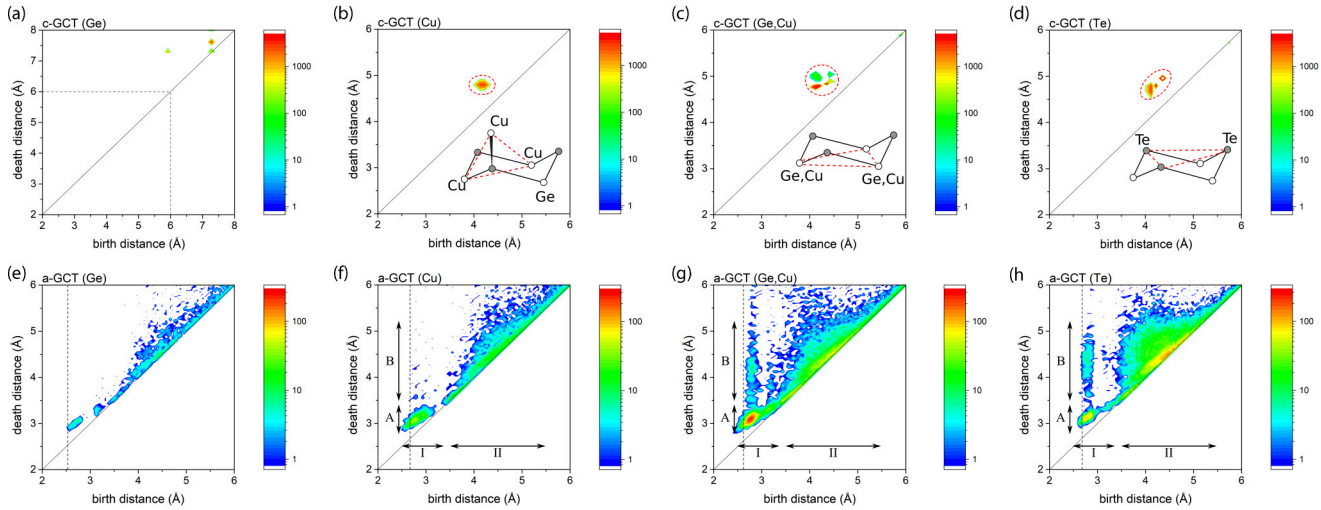

FIG. 6. Persistence diagrams for the crystalline phase (a)–(d), which are Ge-centric (a), Cu-centric (b), Ge- and Cu-centric (c), and Te-centric (d), and in the same order for the amorphous phase (e)–(h). Average bond distances in the amorphous phase are indicated with dashed lines. Intensities are plotted in a logarithmic scale. The insets in (a)–(d) visualize the ring structures in crystalline CGT related to the signals in the PDs.

coordinates indicate that this is a signature of the threefold rings described above—which overproportionally contain Cu, see Fig. 5(b)—and possibly small Cu cluster arrangements. In contrast, the linear "streak" feature in region (I-B) indicates ring structures with short bonds but intermediate sizes. A similar feature was also found for other amorphous structures, and was interpreted as a form of primary ring structures, e.g., in silica [24], which is an indication of the network formation in the system.

The region II at longer birth distances exhibits a broad distribution, with low intensity signals distributed toward long death values, which indicate structures formed by more than four members and which are typically expected in an amorphous phase. However, a close inspection reveals that the signal intensity maxima are distributed around similar coordinates as for the crystalline PD's. This is best seen for the Te-centric PD in (h), where the long curvilinear streak close to the diagonal line is located between birth distances of 4–4.8 Å, which is broadened around the same region as in the crystal (4.1–4.36 Å; see above), but at lower death distances. The distribution of the signals around similar birth values suggests that the associated ring structures are correlated in the amorphous and crystalline states, whereas the signal shift toward the diagonal line indicates that these ring structures are deformed and/or contracted.

E. Structural model of the amorphous phase and relationship to the crystal

To visualize the above descriptions of the amorphous phase, Fig. 7 exemplarily shows sections of the atomic configurations in amorphous CGT obtained from the RMC modeling, highlighting the environments around each element. At a glance, all of the constituent atoms form a random network with coordination numbers of around 2–5. As emphasized in Fig. 7(b), significant amounts of Cu clusters appear in the configurations, where several Cu_3 rings and some chainlike arrangements are formed. Essentially, this is a visual representation of the threefold rings apparent from Figs. 4 and 5 and the Cu clusters indicated in the PDs in region I-A of Figs. 6(f) and 6(g).

Finally, a schematic model of the amorphous structure can be derived from the structural information described so far. This model is aimed at explaining the contrast of the material properties of the two phases. Structurally, the amorphous phase can be thought of as derived from the crystal by small

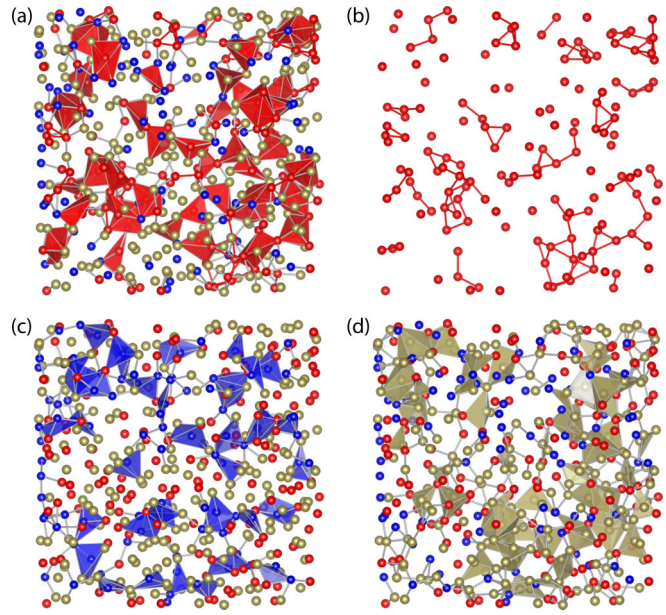

FIG. 7. Atomic configurations extracted from one of the RMC configurations of the same slice with a size of about 32 Å × 32 Å × 13 Å. Atomic environments are highlighted around Cu (a), showing only the Cu clusters and chains (b), and around Ge (c) and Te (d). The colors denote Cu (red), Ge (blue), and Te (gold) atoms.

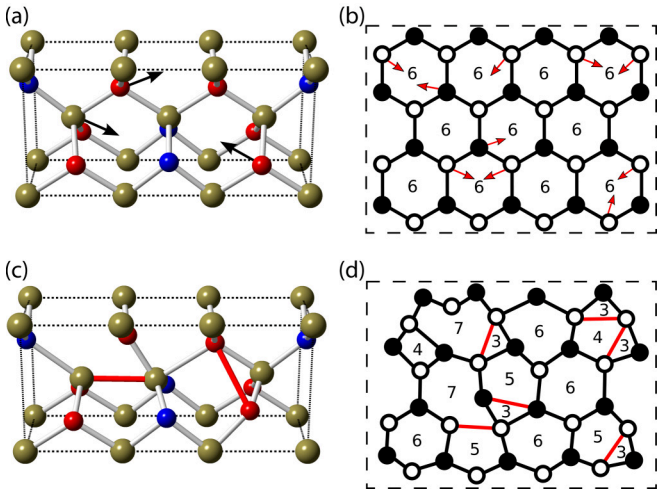

FIG. 8. Relationship between the amorphous and crystalline phase of CGT. The crystal structure is shown in (a) and a schematic representation of the ring structure is shown in (b). The amorphous phase can be rationalized as a deformation of the crystal, with a displacement of the atoms toward the six-ring centers, resulting in new ring structures and the formation of wrong bonds (red) in the amorphous phase, illustrated in (c) and (d). Colors denote Cu (red), Ge (blue), and Te (gold) atoms. Images of the structures were produced using VESTA [49]. In (b) and (d), filled circles denote Te and empty circles are Cu/Ge atoms. The numbers indicate the size of the ring.

movements of the atoms, namely, the movement of atoms (especially Cu) toward the centers of the sixfold rings. These movements are illustrated in Fig. 8(a) for one unit cell and in Fig. 8(b) schematically for the ring structure with arrow symbols. This displacement is directed toward the voids of the crystal structure, leading to the increased coordination numbers of Te and Cu compared to the crystal and (since the interatomic distances do not shrink) to the larger density of the amorphous phase.

The remarkably large coordination number of Cu is also the key to understand the optical properties of this material. It was already pointed out by hard x-ray photoelectron spectroscopy studies [48] and AIMD simulations [16,17,48] that there is an increasing participation of Cu d electrons to the overall bonding, which leads to an increased delocalization of the electrons and thus to a higher electronic polarizability of the material. In turn, this establishes the negative optical contrast of CGT. These findings are corroborated by the present experimental results, which find a high coordination number of Cu, in particular with an increasing metallic character of the bonds (high coordination number of Cu-Cu), and small Cu cluster arrangements, as seen in the Cu PD in Figs. 6(f) and 7(b).

Furthermore, the structural results provide indications to interpret the fast phase-change process in CGT. The considerable rearrangements around Cu may be connected to a higher mobility of the Cu atoms compared to Ge and Te, which was recently indicated by two independent studies using AIMD [18,48]. This mobility is also discussed as a major reason for the fast phase-change speed of CGT. Concomitantly, the atomic displacements lead to a collapse of the sixfold rings. This collapse is indicated from the contraction and distortion of the original ring structures from the shift of the signal maxima in the PDs (Fig. 6), and the ring distribution analysis reveals the formation of smaller ring structures (in particular 3-rings), in which "wrong" bonds of especially Cu-Cu and Te-Te are realized, as visualized in Figs. 8(c) and 8(d). On the other hand, the maximum at $n = 6$ in the ring statistics in Fig. 5 reveals that a significant number of the 6-rings of the crystal structure are conserved, but become largely distorted, as indicated by the wide bond angle distribution in Fig. 4, and by the PDs. The redistribution of chemical bonds also leads to the formation of larger rings sizes with $n \geqslant 7$, schematically indicated in Fig. 8(d). The similar features of the PDs in Fig. 6 furthermore provide evidence that correlated ring structures beyond the nearest-neighbor level exist in both phases. In a nutshell, the fast phase-change process in this material is supported by the fact that the structural reorganization between the crystal and the amorphous phase can be rationalized by small motions of the atoms (which are directed toward the voids in the crystal structure), and by the structural similarities between the amorphous and crystalline phase on the intermediate-range length level.

On the other hand, the involved structural reorganization also has implications for the understanding of the thermal stability [27] of the amorphous phase. The rearrangement of the structure is still substantial, especially concerning the creation of a large number of homopolar bonds and the largely broadened bond-angle distributions, the extensive changes in the local environment of the Cu atoms, and the considerable deformation of the ring structures in the case of the amorphous phase. This significant reorganization acts as an energy barrier that ensures the thermal stability and the long lifetime of the PCM device.

V. CONCLUSION

In conclusion, we present a model for the structure of the amorphous phase of Cu_2GeTe_3, based on a comprehensive experimental approach, using data from AXS and XAFS, modeled by RMC. The resulting structure is analyzed in terms of short- as well as intermediate-range-order parameters. This extensive procedure represents a distinct improvement compared to previous experimental results. We confirmed the formation of smaller ring structures and a large number of homopolar bonds, in agreement with theoretical studies. The emerging view of the structure is used to describe the relationship between the amorphous and the crystalline phase, which can be derived by displacements of atoms (especially Cu) toward the centers of the sixfold rings of the crystal, thereby forming new bonds and resulting in increased coordination numbers and broader distributions of ring structures, but also preserving some structural motifs of the crystal, such as similar interatomic distances and a large ratio of sixfold rings.

The relationship between the amorphous and crystalline phase supports the understanding of the contrast in the phase-change properties, where the structural similarities serve to enhance the phase-change speed in this material, whereas the differences in the chemical bonds, ring structures, and homology establish the density change, the optical contrast, and the thermal stability.

ACKNOWLEDGMENTS

The authors acknowledge partial financial support by the Japan Society for the Promotion of Science (JSPS) Grant-in-Aid for Scientific Research on Innovative Areas "3D Active-Site Science" (No. 26105006). J.R.S. also acknowledges financial support as Overseas researcher under a Postdoctoral Fellowship of JSPS (No. P16796). B.P. thanks the Fond der Chemischen Industrie for financial support. The AXS experiments were performed at BM02 of the ESRF (Experimental No. HC-2213 and No. HC-2534). The XAFS experiments were carried out at BL12C of the KEK-PF (Proposals No. 2010G559 and No. 2012G522). We are indebted to L. Pusztai (Wigner Research Centre for Physics, Hungary and International Research Organization for Advanced Science and Technology, Kumamoto University, Japan) for valuable discussions on the RMC data analysis, and to Y. Saito and S. Shindo (Tohoku University, Japan) for their help with the sample preparation.

[1] M. Wuttig and N. Yamada, Nat. Mater. **6**, 824 (2007).
[2] S. R. Ovshinsky, Phys. Rev. Lett. **21**, 1450 (1968).
[3] Y. Sutou, T. Kamada, M. Sumiya, Y. Saito, and J. Koike, Acta Mater. **60**, 872 (2012).
[4] Y. Saito, Y. Sutou, and J. Koike, Appl. Phys. Lett. **102**, 051910 (2013).
[5] N. Yamada, E. Ohno, K. Nishiuchi, N. Akahira, and M. Takao, J. Appl. Phys. **69**, 2849 (1991).
[6] K. Shportko, S. Kremers, M. Woda, D. Lencer, J. Robertson, and M. Wuttig, Nat. Mater. **7**, 653 (2008).
[7] A. V. Kolobov, P. Fons, A. I. Frenkel, A. L. Ankudinov, J. Tominaga, and T. Uruga, Nat. Mater. **3**, 703 (2004).
[8] B. Huang and J. Robertson, Phys. Rev. B **81**, 081204(R) (2010).
[9] J.-Y. Raty, M. Schumacher, P. Golub, V. L. Deringer, C. Gatti, and M. Wuttig, Adv. Mater. **31**, 1806280 (2019).
[10] J.-Y. Raty and M. Wuttig, J. Phys. D **53**, 234002 (2020).
[11] R. O. Jones, J. Phys.: Condens. Matter **30**, 153001 (2018).
[12] R. O. Jones, Phys. Rev. B **101**, 024103 (2020).
[13] G. E. Delgado, A. J. Mora, M. Pirela, A. Velásquez-Velásquez, M. Villarreal, and B. J. Fernández, Phys. Status Solidi A **201**, 2900 (2004).
[14] P. Jóvári, Y. Sutou, I. Kaban, Y. Saito, and J. Koike, Scr. Mater. **68**, 122 (2013).
[15] K. Kamimura, S. Hosokawa, N. Happo, H. Ikemoto, Y. Sutou, S. Shindo, Y. Saito, and J. Koike, J. Optoelectron. Adv. Mater. **18**, 248 (2016).
[16] J. M. Skelton, K. Kobayashi, Y. Sutou, and S. R. Elliott, Appl. Phys. Lett. **102**, 224105 (2013).
[17] N.-K. Chen, X.-B. Li, X.-P. Wang, M.-J. Xia, S.-Y. Xie, H.-Y. Wang, Z. Song, S. Zhanga, and H.-B. Suna, Acta Mater. **90**, 88 (2015).
[18] A. Koura and F. Shimojo, J. Phys.: Condens. Matter **32**, 244001 (2020).
[19] S. Kohara, K. Kato, S. Kimura, H. Tanaka, T. Usuki, K. Suzuya, H. Tanaka, Y. Moritomo, T. Matsunaga, N. Yamada, Y. Tanaka, H. Suematsu, and M. Takata, Appl. Phys. Lett. **89**, 201910 (2006).
[20] J. Akola and R. O. Jones, Phys. Rev. B **76**, 235201 (2007).
[21] J. Akola and R. O. Jones, Phys. Rev. B **79**, 134118 (2009).
[22] J. Hegedüs and S. R. Elliott, Nat. Mater. **7**, 399 (2008).
[23] H. Edelsbrunner and J. Harer, *Computational Topology: An Introduction* (American Mathematical Society, Providence, RI, 2010).
[24] Y. Hiraoka, T. Nakamura, A. Hirata, E. G. Escolar, K. Matsue,, and Y. Nishiura, Proc. Natl. Acad. Sci. (USA) **113**, 7035 (2016).
[25] M. Murakami, S. Kohara, N. Kitamura, J. Akola, H. Inoue, A. Hirata, Y. Hiraoka, Y. Onodera, I. Obayashi, J. Kalikka, N. Hirao, T. Musso, A. S. Foster, Y. Idemoto, O. Sakata, and Y. Ohishi, Phys. Rev. B **99**, 045153 (2019).
[26] Y. Onodera, S. Kohara, S. Tahara, A. Masuno, H. Inoue, M. Shiga, A. Hirata, K. Tsuchiya, Y. Hiraoka, I. Obayashi, K. Ohara, A. Mizuno, and O. Sakata, J. Ceram. Soc. Jpn. **127**, 853 (2019).
[27] Y. Saito, Y. Sutou, and J. Koike, J. Phys. Chem. C **118**, 26973 (2014).
[28] S. Hosokawa, W.-C. Pilgrim, J.-F. Bérar, and S. Kohara, Eur. Phys. J.: Spec. Top. **208**, 291 (2012).
[29] J. Krogh-Moe, Acta Crystallogr. **9**, 951 (1956).
[30] N. Norman, Acta Crystallogr. **10**, 370 (1957).
[31] Y. Waseda, *Novel Application of Anomalous (Resonance) X-Ray Scattering for Structural Characterization of Disordered Materials* (Springer, Berlin, 1984).
[32] S. Hosokawa, I. Oh, M. Sakurai, W.-C. Pilgrim, N. Boudet, J.-F. Bérar, and S. Kohara, Phys. Rev. B **84**, 014201 (2011).
[33] J. R. Stellhorn, S. Hosokawa, and W.-C. Pilgrim, Z. Phys. Chem. **228**, 1005 (2014).
[34] S. Hosokawa, Y. Wang, J.-F. Bérar, J. Greif, W.-C. Pilgrim, and K. Murase, Z. Phys. Chem. **216**, 1219 (2002).
[35] A. L. Ankudinov, B. Ravel, J. J. Rehr, and S. D. Conradson, Phys. Rev. B **58**, 7565 (1998).
[36] O. Gereben, P. Jóvári, L. Temleitner, and L. Pusztai, J. Optoelectron. Adv. Mater. **9**, 3021 (2007).
[37] O. Gereben and L. Pusztai, J. Comput. Chem. **33**, 2285 (2012).
[38] P. Pyykkö, Phys. Rev. B **85**, 024115 (2012).
[39] P. Jóvári, I. Kaban, J. Steiner, B. Beuneu, A. Schöps, and M. A. Webb, Phys. Rev. B **77**, 035202 (2008).
[40] S. Hosokawa, J.-F. Bérar, N. Boudet, W.-C. Pilgrim, L. Pusztai, S. Hiroi, K. Maruyama, S. Kohara, H. Kato, H. E. Fischer, and A. Zeidler, Phys. Rev. B **100**, 054204 (2019).
[41] B.-K. Teo and P. A. Lee, J. Am. Chem. Soc. **101**, 2815 (1979).
[42] J. Akola, J. Larrucea, and R. O. Jones, Phys. Rev. B **83**, 094113 (2011).
[43] P. Jóvári, I. Kaban, J. Steiner, B. Beuneu, A. Schöp, and A. Webb, J. Phys.: Condens. Matter **19**, 335212 (2007).
[44] S. L. Roux and P. Jund, Comput. Mater. Sci. **49**, 70 (2010).
[45] M. Micoulaut, A. Piarristeguy, H. Flores-Ruiz, and A. Pradel, Phys. Rev. B **96**, 184204 (2017).
[46] S. Grimme, J. Comput. Chem. **27**, 1787 (2006).
[47] S. Hosokawa, W.-C. Pilgrim, A. Höhle, D. Szubrin, N. Boudet, J.-F. Bérar, and K. Maruyama, J. Appl. Phys. **111**, 083517 (2012).
[48] K. Kobayashi, J. M. Skelton, Y. Saito, S. Shindo, M. Kobata, P. Fons, A. V. Kolobov, S. Elliott, D. Ando, and Y. Sutou, Phys. Rev. B **97**, 195105 (2018).
[49] K. Momma and F. Izumi, J. Appl. Crystallogr. **44**, 1272 (2011).